GEMINI
8-M Telescopes Project

RPT-O-G0046

f/16 IR Secondary Structural Analysis Results

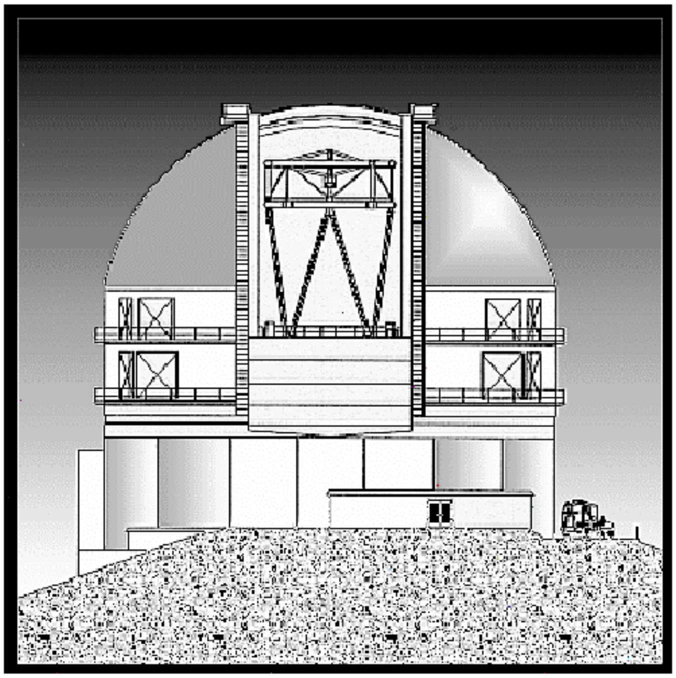

Eric Hansen
Opto-Mechanical Engineer

June 13, 1994

GEMINI PROJECT OFFICE 950 N. Cherry Ave. Tucson, Arizona 85719
Phone: (602) 325-9329 Fax: (602) 322-8590

Table of Contents

Section		Page No.
1	Introduction	1
2	Gravity Deflections	3
3	Polishing Residuals	4
4	Wind Loading	4
5	Thermal Deformations	5
6	Mirror Seeing	7
7	Stresses and Failure Analysis	7
8	Dynamic Analysis	9
9	Conclusions	11
10	References	11

PRELIMINARY

f/16 IR Secondary Structural Analysis Results

1. Introduction

This report outlines the scope and results of a preliminary structural analysis for the f/16 IR secondary mirror. The purpose of this effort was to predict the static and dynamic performance of a novel design made from silicon carbide. The mirror blank is a lightweighted structure 1023 mm in diameter and 155 mm in height with a weight of 40 Kg. The optical surface is a convex hyperboloid with a base radius of curvature of 4193.0685 mm and conic constant of -1.613. The mirror has a 168.0 mm diameter central hole that serves as a pupil stop, minimizing the non-reflecting surfaces seen by the IR instruments. The secondary will be articulated for chopping and rapid wavefront tilt correction.

The secondary mirror assembly will be capable of two axis square wave chopping with a focal plane amplitude of up to 15 arcsec total image motion at 10 Hz and 80% duty cycle, and up to 30 arcsec image motion at 5 Hz with 80% duty cycle. The overall image quality during dwell time must have 50% encircled energy within 0.4 arcsec at 10 um.

The secondary will also be capable of two axis active tilt for image motion compensation. This is required to remove telescope wind buffeting motion and enclosure vibrations as well as the tilt power of the incoming wavefront to negligible levels. This may require motions in the focal plane of +/- 1 arcsec up to 8 Hz with a 3 dB drop off at 8 Hz. In addition tilts up to 40 Hz may be required to correct for resonances in the telescope structure. The overall image quality requirement at 2.2 um wavelength is 50% encircled energy within 0.1 arcsec diameter and 85% encircled energy within 0.25 arcsec diameter zenith pointing and increasing with the secant of the zenith angle to the 0.6 power. Note that both the 2.2 and 10 um specifications are system requirements and include primary, enclosure, tracking, etc. effects. The budget allocations for the secondary mirror are shown in Table 1.

Table 1 f/16 Image Quality Error Budget

Secondary Mirror Error Source	50% @ 2.2 um	85% @ 2.2 um	85% @ .55 um (goals)	50% @ 10 um
Polishing Residuals	0.015	0.067	0.11	0.015
Support Residuals*	0.01	0.022	0.033	0.03
Thermal Distortion	0.01	0.009	0.013	0.005
Wind Buffeting*	0.01	0.018	0.02	0.01
Mirror Seeing**	.004	0.027	0.02	.004
Plate Scale Change***	50 ppm	50 ppm	50 ppm	50 ppm

Image Quality Degradation in arcseconds diameter

* Zenith angle dependent (given for zenith pointing and high wind conditions)

** Total budget shared with chopper

*** No active correction planned

The mirror blank is a lightweight silicon carbide structure that consists of a 5 mm facesheet and 3 mm triangular core 'eggcrate' ribs whose height varies with mirror radius to minimize self weight deflection. The blank has a rotational inertia of 2.5 kgm^2 about its center of gravity (CG), and is shown in Figure 1. One advantage of this material is that its high specific stiffness allows a three point support in the plane of the CG with minimum print through to the mirror surface. In addition, the lightweight design allows both a short thermal time constant with low thermal distortion and high frequency active correction and chopping with reasonable actuator loads.

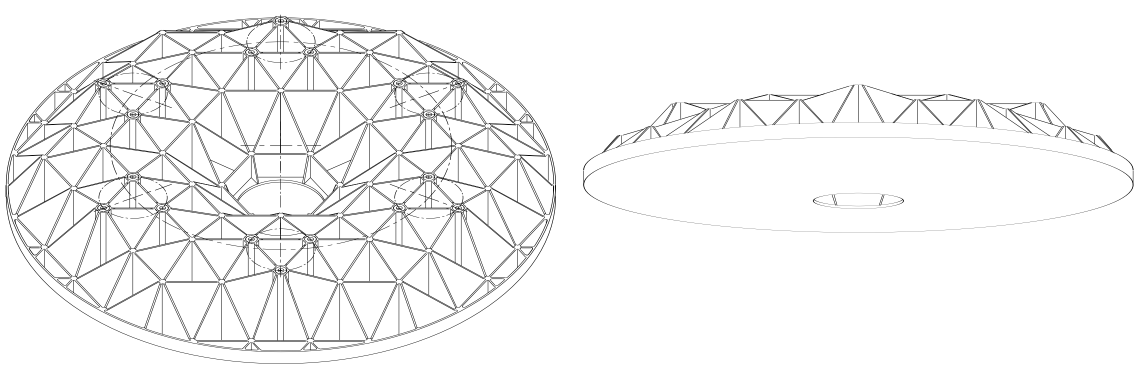

Figure 1 Secondary Mirror

The general analysis method used is similar in all structural deformation cases, I-DEAS finite element analysis is used to produce stress values or nodal displacement files which are transformed into Code V compatible grid files and superimposed on the nominal telescope prescription in order to calculate encircled energy diameters. For cases involving small deformations, which produce unreliable Code V results, the deformations were scaled up to a 40 nm rms level and the encircled energy increase scaled down by the same factor.

A number of vendors using different processes are capable of fabricating the mirror blank. Each process produces a material with different mechanical properties, some of these are shown in Table 2.

Table 2 Material Properties

Vendor	Density (kg/m^3)	Elastic Modulus (GPa)	Thermal Conductivity (W/mC)	CTE (ppm/C)	Fracture Toughness K_{IC} (MPa $m^{.5}$)
Carborundom	3,100	366	95	2.5	na
UTOS	2,920	311	156	2.6	2.5
Morton CVD	3,210	466	250	2.4	2.7-3.3
Lockheed / VSOI	3,050	390	185	2.5	3.6

Material properties used for the analysis are based on reaction bonded silicon carbide material and are as follows;

Young's Modulus	350 GPa
Density	3100 kg/m3
Specific Heat	670 J/kg C
Conductivity	156 W/m C
CTE	2.5 ppm/C

Analysis results are reviewed in the following sections; 2. gravity deflections, 3. polishing residuals, 4. wind loading, 5. thermal deformations, 6. mirror seeing, 7. stresses and failure analysis, and 8. dynamic analysis.

2. Gravity Deflections

The mirror figure will be optimized for zenith pointing, with print through effects polished out at that orientation. This implies that the mirror will be tested face down, and that gravity induced lateral deformation and negative axial deformation will be introduced with increasing zenith angle.

Gravity induced distortion was evaluated using three place bipod support of the mirror blank at a 63% radius. This value minimizes deformation due to axial gravity loading. Axial mounting locations were also optimized by minimizing the horizon pointing surface deformations. This information also gives an indication of the sensitivity in location of the support points for assembly purposes. The supports were designed to match the planned spring rates for combined flexures and mounting brackets with an axial stiffness of 3.64 E8 N/m and lateral stiffness of

5.63 E7 N/m. Surface deformations were found for gravity loading at various zenith angles. The results are given in Table 3, and surface contours are given in Figure 2.

Because gravity induced surface deformations on the secondary are predictable, an improvement in image quality can be made when the primary active supports are used to correct wavefront errors by matching the gravity induced deformations on the secondary surface. The results of active optics correction are also shown in Table 3. An encircled energy increase of 0 indicates the analysis yielded a slight decrease in encircled energy diameter.

Table 3 Gravity Deflection Effects

	Zenith Angle (deg)		
	25	45	75
Surface Deflection RMS (nm)*	6.8	15.8	35.3
50% EE Increase (arcsec) / Budget**	.0031 / .015	.0078 / .025	.020 / .065
85% EE Increase (arcsec) / Budget**	.0121 / .036	.0303 / .061	.0667 / .161
50% EE Increase after Correction (arcsec)	0	.0004	0
85% EE Increase after Correction (arcsecs)	.0009	.0019	0

*Surface deformations with tilt, piston and focus removed

**Encircled energy increase at 2.2 um, on axis, analysis includes diffraction

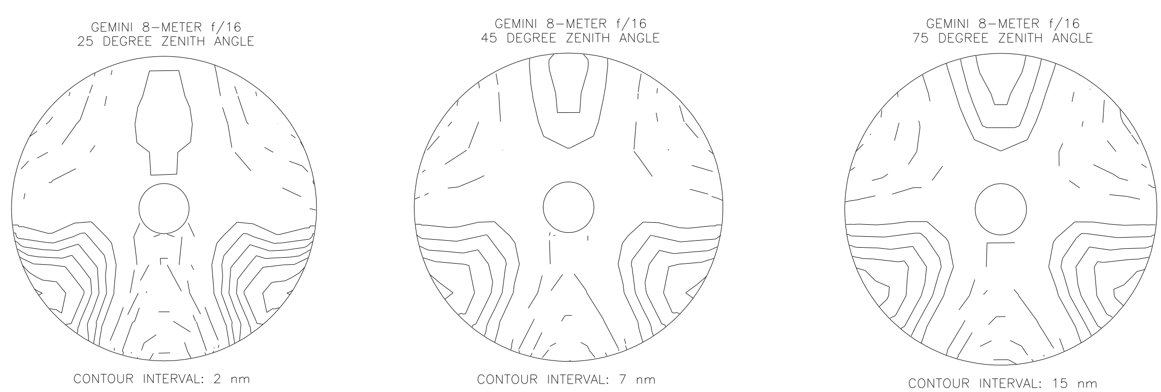

Figure 2 Gravity Deformation Surface Contour Maps

It is expected that fabrication and assembly tolerances will produce residual mounting loads between the mirror mount and blank. These loads will induce strains in the blank that will effect image quality. To predict the effect, unit force and moment loads were applied to the mirror model and resulting encircled energies were found. The results showed that the expected mismatches will produce image quality reductions that are well within tolerance.

3. Polishing Residuals

Polishing pressure applied to structured mirrors results in intercellular bowing. This 'quilting' is due to the difference in faceplate stiffness between areas over ribs as compared to areas between ribs, and leaves the optical surface with a quilted deformation pattern. A regular cell pattern results in satellite images in the focal plane with positions and amplitudes that are functions of quilting spatial frequency and amplitude. Using finite element analysis it was found that the 0.5 psi polishing pressure typical of bare silicon carbide produces 30 nm peak to valley, or 8 nm rms deviations on the surface. CodeV was then used to find the resulting intensity distribution in the focal plane. Because the number of secondary mirror cells is approximately equal to the number of actuators on the primary, it was found that the sensitivity to quilting is similar to that from support print through on the primary. With an 8 nm rms surface, the image quality meets the satellite image specification of $I_s \leq I_c\, r^{-3}(5x10^{-4})$, where I_S is the intensity of the satellite image, I_C is the central intensity in the point spread function, and r is the radial distance of the satellite image from the center of the point spread function in arc seconds. Gravity produces the same quilting pattern, but the amplitude produced by 1g is a negligible 0.27 nm rms.

4. Wind Loading

Wind loading on the mirror will both deform the mirror from it's ideal shape and displace it from its correct position. The effect of uniform and nonuniform wind loading was evaluated by loading the mirror face with the stagnation pressures of different wind speed profiles and evaluating the surface deformation using finite element analysis.

The maximum windspeed expected at the secondary is 7 m/s, this yields a uniform surface loading of 16 Pa, and produced a deformation of 1.48 nm rms, with the same three lobed pattern as axial gravity deflection. The increase in 50% encircled energy from this deformation is .0008 arcsec. This compares to the current error budget allotment of .010 arcsec for all secondary wind effects.

A nonuniform wind loading pattern shape similar to that used for primary modeling was also used. It is based on a 1982 F. Forbes and G. Gabor report[1] listing data taken at the MMT on Mt. Hopkins in a zenith pointing condition. The pressure varied from 0 to 3 Pa which resulted in a secondary surface deformation of .45 nm rms, the surface contour is shown in Figure 3. These results reflect a stiff mirror and indicate that wind loading will not be significant in comparison to gravity or dynamic loading of the mirror blank.

Figure 3 Nonuniform Wind Pressure Deformation Contour Map

5. Thermal Deformations

Temperature changes and thermal gradients within the mirror blank will act to deform the mirror surface. Silicon carbide has high thermal conductivity and relatively low coefficient of thermal expansion. These properties reduce thermally induced strains and subsequent image degradation as compared to other mirror materials. Uniform temperature changes result primarily in a change in radius of the mirror surface. The focus correction capacity of the telescope removes this effect automatically with only a small resultant change in image plate scale. Estimates were made of the maximum thermal gradients within the blank from sources such as actuators, convective heat transfer to the atmosphere and radiative heat transfer to the night sky using TMG, a finite difference thermal analysis software. The surface figure change due to these gradients was evaluated using finite element analysis and deformations transferred to Code V for image quality analysis. The model uses a typical case of 2 m/s wind speed, a -0.2 degree per hour nighttime ambient air temperature decline, one watt heat input to the mirror from each mounting point and an initial temperature difference of 0.5 C between air and mirror when the dome opens. The results in terms of image quality are given in Table 4 with surface deformation after 12 minutes shown in Figure 4.

From these results it is clear that thermal gradients on the secondary could pose a risk to telescope performance, and active correction of longer term deformations will be required. Note that thermal deformations are of low spatial frequency and well within the bandwidth of active control. The results of active optics correction are also shown in Table 4.

12 minute exposure | Tilt focus piston removed | Wavefront after active optics

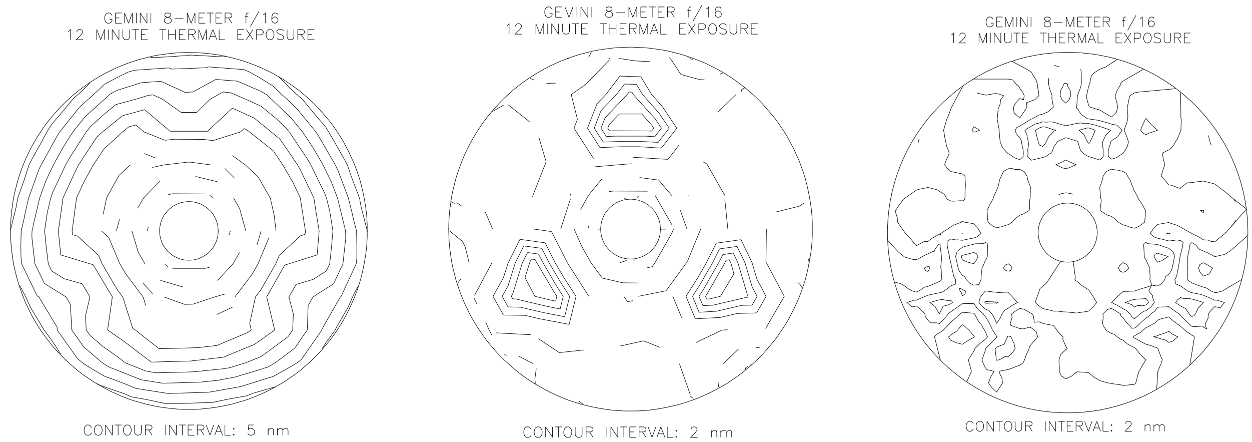

surface contour | surface contour
correction
20 nm rms (surface) | 4.6nm rms (surface) | 1.8 nm rms (wavefront)

Figure 4 Thermal Deformations Before and After Correction

Table 4 Thermal Deformations

		After Time of	
	Budget	12 minutes	12 hours
Surface Deflection RMS (nm)*		4.6	123
50% EE Increase (as) **	.005	.0023	.0143
85 % EE Increase (as) **	.009	.0106	.062
Plate Scale Change (ppm)	50	0.72	25
Active Correction Force Required (N)	10	7.6	8.3
50% EE Increase after Correction (arcsec)		.0004	.0012
85% EE Increase after Correction (arcsec)		.0018	.0039

*Surface deformations with tilt, piston and focus removed

**Encircled energy increase at 2.2 um, on axis, analysis includes diffraction

6. Mirror Seeing

In order to predict the level of image quality degradation due to secondary mirror seeing a model has been set up to evaluate the mirror to air temperature difference under observatory conditions. Transient heat transfer to, from and through the secondary mirror was modeled using one dimensional finite difference methods. The model's response to night time ambient air temperature profiles recorded on Mauna Kea by UKIRT and expected enclosure temperatures during the day was then found. By scaling correlations used to estimate primary mirror seeing for diameter and slope error sensitivity, the relationship between increase in encircled energy and mirror air temperature difference was determined. The relation used in the model was 50 % encircled energy increase, in arc seconds, due to seeing as $.0086\ \Delta T^{6/5}$, with temperature in degrees C. The percentage of time during observing that secondary mirror seeing was below specific levels was then found for 303 days of temperature data.

There are many parameters within the model that can be varied to adjust the performance of the system. These parameters include wind speed, mirror heating due to the articulation mechanism, and temperature prediction errors. The seeing error budget changes as a function of wind speed, this is due to the trade off that can be made between seeing and wind shake errors. Therefore, the analysis was done at windspeeds of 1, 3 and 5 m/s with seeing error budgets of .002, .004 and .008 arcseconds respectively.

Prediction of the beginning of night temperature was done using two different methods. Perfect prediction, which assumes accurate knowledge of starting temperatures and carbon copy, which begins the analysis with the secondary at the beginning temperature of the previous night, were used. It was found that temperature prediction is not critical for the secondary because of the short thermal time constant. The mirror quickly equalizes in temperature with the ambient air.

The positioning actuators for the secondary mirror will be electrically driven. This implies that some amount of heat will be transmitted to the mirror blank. The analysis used values corresponding to 0, 0.8 and 1.6 watts per actuator. This factor had a substantial effect at low wind speeds where excess heat is more difficult to reject to the ambient air.

Averaging the results for temperature prediction and heat input levels, and using Mauna Kea wind speed distributions from CFHT, it was found that the total time within specification for secondary mirror seeing was 85% under realistic operating conditions.

7. Stresses and Failure Analysis

The mirror blank is subject to stress as a result of angular accelerations from chopping and gravity, as well as thermal growth mismatch with the mount. Stresses are concentrated in the area of the mounting points for all cases. For this reason, a more detailed model of the mounting area was made. This model is shown in Figure 5.

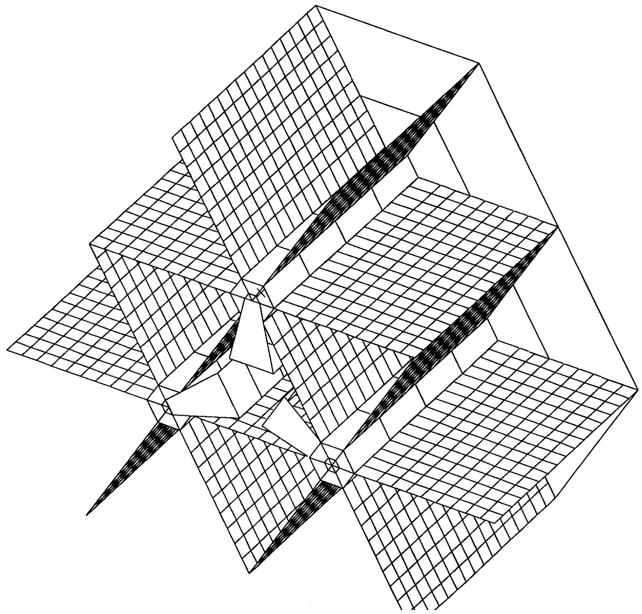

Figure 5 Mounting Point Finite Element Model

The mount model consists of a section of the mirror face and associated ribs along with invar studs and bracket. This bracket connects the support point, located close to the plane of the center of gravity, to three studs projecting from the rear surface of the mirror.

The design offers three significant advantages. First the three point mounting better distributes the support loads, giving a 10% reduction in zenith pointing self weight deflection as well as reduction in mounting point stresses. Second, it allows more convenient attachment at the rear of the mirror while effectively supporting it close to the C.G. plane for minimum horizon pointing deflections. Third, it is configured to allow differential expansion rates between the invar and Silicon carbide with minimum impact on the mirror. The maximum principle stresses calculated for different loading conditions are listed in Table 5.

Table 5 Maximum Principle Stress Levels

Loading Condition	Location / Material	Model	Maximum Stress (MPa)
8 G’s lateral (static)	Ribs / SiC	Mirror	2.0
8 G’s lateral (static)	Collar / SiC	Mount	56.0
8 G’s lateral (static)	Bracket / Invar	Mount	241
-30 C temperature change	Collar / SiC	Mount	3.0
Chopping (400 N axial, static)	Ribs / SiC	Mount	1.2

The stress levels within the structure are critical because of the brittle nature of the material. Potential failure modes of silicon carbide are fast fracture and slow crack growth. Slow crack growth of silicon carbide has been examined by the University of Dayton[2] with the conclusion that slow crack growth is not a mode of failure at room temperature below 150 MPa. Maximum allowable stresses were then defined based on fast fracture, using a statistical approach. Weibull statistical properties were used to determine the probability of failure under design stresses. The properties used are listed below;

Weibull Modulus	18.6
Scale Factor	145.1 MPa $m^{2/18.6}$

Using this data the probability of failure, under 8g loading, is less than 1 in 1,000,000.

Maximum allowable stresses were also defined using a material toughness approach. The fundamental principle of fracture mechanics is that the stress field ahead of sharp cracks can be characterized in terms of a single parameter K, the stress intensity factor. This parameter is related to both stress level and flaw size for a given geometry. When the particular combination of stress and flaw size reaches a critical value of stress intensity, unstable crack growth occurs. All three of these basic factors are interrelated in brittle fracture. All other factors such as temperature, loading rate, residual stress, etc. merely affect the above three primary factors.

Data indicates that the stress intensity factor for reaction bonded silicon carbide can vary from 2.5 to 5.0 $x10^6$ $N/m^{1.5}$. Using the plate geometry of the ribs, with a maximum defect size comparable to the rib thickness, results in a maximum allowable stress of 23 MPa before crack growth occurs. For all analysis done up to this point maximum principle rib stresses have been below 2 MPa. This includes both static and dynamic conditions.

8. Dynamic Analysis

In an effort to correct pointing errors and improve IR sensing the mirror will be required to undergo a number of rapid chopping and tip-tilt motion profiles. This active positioning will deform the mirror surface as compared to a static case and will reduce image quality. The magnitude of this distortion has been evaluated separately for chopping and tip-tilt at various frequencies. The effect on image quality has been analyzed and compared to the nominal case.

The first mode of vibration dominates dynamic response. Natural frequencies of the mirror blank were found for a number of restraint conditions. On a three point kinematic mount the first mode was found to be 638 Hz. With the inclusion of mount brackets and flexures the first resonance drops to 202 Hz, a factor of 5 above the highest control frequency.

Previous studies examined two separate cases of chopping, the first rotated the mirror about it's center of gravity about an axis parallel to the elevation axis, or horizontal axis. The second case rotated the blank about it's CG on an axis orthogonal to the first, or vertical axis. The vertical axis lies above one mirror mounting point. Results indicated that the worst case deformation came from chopping about the horizontal so only that loading case was analyzed.

The deformations were found using a static loading to simulate the dynamic response of the mirror. Because the first mode of the mirror is well separated from the chopping frequency the deformation of that mode will be close to the deformation caused by the maximum acceleration applied statically. Due to the 80% dwell requirement on the chopping motion, the effective chopping frequency for a 10 Hz chop can be modeled as 50 Hz. For a sinusoidal chopping profile at 50 Hz effective frequency, the peak acceleration is 16 r/s^2. When the axial force component is applied statically to the mirror as a pressure, a 1.0 um P-V deformation results.

The results shown in Table 5 combine a figure error with a rigid body tilt of the mirror on the three mounting flexures. Previous studies have shown that for chopping, the peak deflection is reduced by a factor of 10 after the applied chopping force is removed and observation begins, for tip-tilt correction, however, this reduction does not apply. In addition, the rigid body tilt is a harmonic oscillation that smears an averaged image and increases the effective encircled energy. Both these factors are accounted for in the encircled energy calculations. The worst case surface deformation during observation is shown in Figure 6. Note that 66 arcseconds of mirror motion produces 15 arcseconds image motion.

Table 5 Dynamic Deformations and Image Degradation

Mirror Motion (analysis wavelength)	Peak Actuator Force (N)	Peak Surface Deformation (nm RMS)	Increase in 50% EE Tilt + deformation / Budget (arcsec)
10 Hz 66 arcsec chopping (@ 10 um)	125	538	.044 / .047
5 Hz 132 arcsec chopping (@ 10 um)	63	269	.022 / .047
8 Hz 8.0 arcsec correction (@ 2.2 um)	0.39	17	.0017 / .011
40 Hz 0.4 arcsec correction (@ 2.2 um)	0.49	21	.0021 / .011

Damping of the mirror blank will be required so that the ringing amplitude will not increase after multiple chopping or tip tilt cycles. It was found that the .5% damping expected of the mounted mirror is sufficient to reduce ringing to a negligible level over the 10 Hz chopping dwell time of .04 seconds. One supplier of reaction bonded material, United Technologies Optical Systems[3] uses 0.2% damping for modeling their reaction bonded materials and have measured up to 18% damping on mounted SiC mirror blanks.

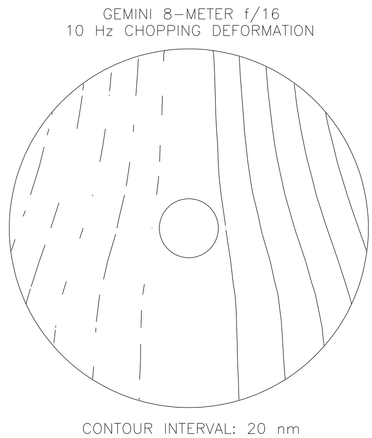

Figure 6 Chopping Deformation Contour Map

9. Conclusions

The analysis done to date shows no problems that would compromise the required performance, and in most cases meets the budget without the aid of active optics. The two areas of greatest concern are thermal gradients across the blank and mount stiffness. This study covers only the performance of the secondary mirror. It does not yet include the flexibility of drive mechanisms. While the results show no problems associated with the mirror blank, the design of the secondary system including mounts and drivers must mature before these areas can be adequately studied to assure meeting the required system performance.

10. References

1. Forbes, Gabor, *Wind loading of large astronomical telescopes*, SPIE, Vol 332, March 1982
2. Personal communication, George Graves, University of Dayton (Ohio) Research Institute
3. Personal communication, Robert Jeager, United Technologies Optical Systems